For the typeset version please see: https://doi.org/10.1016/j.epsl.2023.118382

Cite as: Pieterek, B. and Jones, T.J., 2023. The evolution of Martian fissure eruptions and their plumbing systems. *Earth and Planetary Science Letters*, 621, 118382. doi:10.1016/j.epsl.2023.118382

The evolution of Martian fissure eruptions and their plumbing systems

Bartosz Pieterek[1*], Thomas Jones[2]

[1]Geohazard Research Unit, Institute of Geology, Adam Mickiewicz University in Poznań

[2]Lancaster Environment Centre, Lancaster University, Lancaster LA1 4YQ, UK

*Corresponding author: barpie@amu.edu.pl; phone: +48 693290465

Abstract: **203** words
Main text: **6429** words
References: **73**
Tables: **1**
Figures: **7**
Supplementary tables: **3**
Supplementary figures: **34**
Supplementary Data: **1**

Abstract

On Earth, the investigation of fissure eruptions and their deposits provide fundamental insights into the evolution of the subsurface volcanic plumbing system. On Mars, we have limited evidence of the spatiotemporal evolution of fissure-fed volcanic systems, and thus the processes operating within their subsurface-feeding dykes remain poorly understood. The timescales of eruptive activity and the longevity of the associated plumbing systems remain unknown for Martian fissure-fed volcanism. Here, we performed high-resolution mapping and age dating of a ~ 90-km long volcanic fissure system to uniquely unravel the evolution of the volcanic eruptions and the associated plumbing system both spatially and temporally. We show that through time, eruptive activity evolved from highly mobile lava flows that erupted along the entire fissure length to viscous lava flows that erupted at a single location and built up a cone. These observations suggest that the subsurface plumbing system became more chemically differentiated and the magma flow localized from a dyke-like, linear source to a point source with time. Our detailed reconstructions also suggest a long-lived (at least $\gtrsim$ 9 Ma), and active volcanic plumbing system. Therefore, we argue that spatiotemporal mapping constitutes a powerful approach to understand the dynamic nature of subvolcanic plumbing systems on planetary bodies.

Keywords: Fissure eruption, Tharsis, Magma convection, Eruption longevity, Igneous plumbing system, Eruptive history

Introduction

The spatiotemporal investigation of volcanic edifices on Mars provide direct insights into, the otherwise inaccessible, magmatic or subvolcanic plumbing systems (Pieterek et al., 2022; Richardson et al., 2021, 2017). On Earth, the dynamics of magma in the plumbing system exhibits a fundamental control on the style, behaviour, and longevity of eruptions (Gonnermann and Manga, 2007; Houghton et al., 2004; Jones and Llewellin, 2021). Both on Earth and Mars different eruptive styles yield different volcanic products and thus are expressed by various morphologies of volcanic landforms (de Silva and Lindsay, 2015; Jones et al., 2022; Siebert et al., 2015; Wilson and Head, 1994). Therefore detailed observations of these volcanic products and landforms from remotely sensed data provide a means to unravel volcanic eruption history on other planets and satellites (Bleacher et al., 2007; Hauber et al., 2009; Peters et al., 2021). Here, we focus on reconstructing the eruptive history of fissure eruptions on the planet, Mars.

Fissure eruptions occur when an ascending dyke intersects the surface and/or when magma exploits a pre-existing fault system. The associated eruptive geometries are therefore of high-aspect ratio. On Earth, volcanic fissures typically erupt magmas that are basaltic in composition, however, magmas spanning the compositional spectrum from ultramafic (Brown et al., 2012) to rhyolite (Lara et al., 2006) have been documented. Fissure eruptions on Earth occur at a wide range of scales, from highly voluminous (e.g., 10^5 to 10^7 km^3) outpourings associated with large igneous provinces (Black et al., 2021; Brown et al., 2014; Thordarson and Self, 1993) to frequent mafic volcanism across the globe (Valentine and Gregg, 2008). Irrespective of their eruption location or size, all fissure eruptions can provide insights into the subsurface plumbing system. For example, fissure eruptions localize from a high-aspect ratio erupting geometry (i.e., eruption all along the fissure's strike) to a (singular) point source with time. The cause of this localization is complex and can result from a wide range of interconnected processes, these include the thermo-rheological effects and magma solidification within the feeder dyke (Bruce and Huppert, 1990, 1989; Wylie et al., 1999), extensive microlite crystallization in stagnation zones (Moreland et al., 2019), along strike variations in dyke width (Ida, 1992), progressive edifice loading and focussing along dyke intersection zones (Cocchi et al., 2019), localized magma flow patterns generated by subsurface convective exchange (Jones and Llewellin, 2021), and the interaction with surface lava flows causing in-vent ponding and stagnation (Jones et al., 2017). Furthermore, in the case of the 2018 Lower East Rift Zone eruption of Kīlauea (Neal et al., 2019), near real-time petrological analysis revealed the systematic mixing between magmas of different age and composition within the plumbing system (Gansecki et al., 2019).

On Mars, such analysis and investigation of fissure eruptions and their accompanying magmatic plumbing systems are solely limited to remotely sensed data. To date, the majority of Martian studies have focused on regional-scale (e.g., Tharsis) plumbing system(s) reconstructions (Hauber et al., 2009; Pieterek et al., 2022; Richardson et al., 2021), rather than reconstructing individual volcanic units or

eruption events at the local-scale. One of the most comprehensive spatiotemporal, local-scale studies conducted on Mars was on the summit caldera volcanism of Arsia Mons (Richardson et al., 2017). This revealed that prolonged volcanism began at 300–200 Ma with peaks in activity around 150 and 100 Ma, after which the volcanism waned until the final eruptive vents were formed at 90–10 Ma. Such temporal reconstruction reveals the possibility for long-lived volcanic systems beneath Arsia Mons. This might also be assumed for other Martian volcanic fields but these not been explored in detail.

The comparison with terrestrial counterparts can provide fruitful insights into Martian volcanic systems. For example, by analysing eruption conditions of mapped lava flows in Tharsis, it has been shown (Peters et al., 2021) that Martian lava flows are much larger in volume and are erupted over greater lengths of time. This is in agreement with theoretical considerations (Wilson and Head, 1994), that suggest feeder dykes remain active and open for longer time periods relative to terrestrial volcanoes (Peters et al., 2021). Moreover, the life cycle of Tharsis Montes magma production has been inferred (Bleacher et al., 2009) to be at least an order of magnitude longer than for shield volcanoes on Earth. Such documented longevity of the Martian volcanic systems, supports increased timescales for magmatic evolution and differentiation within the plumbing system, changing the physical properties of the erupted magma and thus the associated lava flow morphologies and surficial landforms.

Although volcanism on Mars is thought to be dominated by eruptions of basaltic composition, studies of Martian meteorites (Udry et al., 2020) and *in-situ* rover-conducted investigations (Mangold et al., 2017) indicate variable igneous rock compositions, likely resulting from magma differentiation. The extent to which magma differentiation occurs during the eruption of (long-lived) volcanic systems on Mars remains an open question. Moreover, we do not fully understand how Martian fissure-fed volcanic fields and their associated plumbing systems evolve both spatially and temporally. Thus, we do not understand typical eruption timescales (durations of eruption phases, quiescent periods, and total lifetime) nor do we understand how eruption style (explosive vs effusive) can vary between successive eruptions. This is, at least in part, due to the lack of contemporary eruption observation data and the limited petrological information – we are largely limited to orbital-based observations. However, here, applying the combination of the Context Camera images and digital elevation models, we conducted high-resolution mapping and age dating to provide a detailed spatiotemporal investigation of the fissure system south of Pavonis Mons, Mars. This has enabled us to reconstruct the eruptive evolution of a Marian fissure system and place quantitative constraints on the lifetime and lengthscales of Martian fissure-controlled plumbing systems.

Geological setting

In the Tharsis Volcanic Province on Mars, the major volcanoes (e.g., Olympus Mons, Alba Mons, and Tharsis Montes) are accompanied by hundreds of smaller and likely dyke-fed volcanoes and vents with associated lava flows that are unevenly distributed forming volcanic clusters (Hauber et al., 2011,

2009; Pieterek et al., 2022; Richardson et al., 2021). Clustering is reflected by a grouping of edifices that locally overlap and form local volcanic fields. Based on their spatial distribution, edifice elongations and vents alignments in relation to giant volcanoes, they can be grouped into radially and circumferentially dyke-fed volcanoes (Pieterek et al., 2022; Richardson et al., 2021). The highest concentration of the Tharsis volcanoes occurs to the south and southeast of Pavonis Mons. They occur in NNE-trending alignments interpreted to be controlled by the regional tectonic trend (Hauber et al., 2009) and magmatically sourced from the Pavonis Mons-related plumbing system (Pieterek et al., 2022) or underplating magma emplaced at the crust-mantle boundary beneath the southeastern region of Tharsis Montes (Richardson et al., 2021). Morphological analyses (Hauber et al., 2009) of volcanic edifices and associated landforms have illustrated similarities with terrestrial basaltic volcanic fields, where the most typical landforms of Martian plains-style volcanism are low shield volcanoes and fissure vents associated with lava flows. Given the volcanic edifices are a few hundred meters high with large basal areas with diameters typically several up to ~ 50 km, they form extremely low-angle flank slopes (< 1°) indicating the construction by low viscosity magmas which are predominantly basaltic in composition (Hauber et al., 2011, 2009; Mangold et al., 2010; Peters et al., 2021).

The Tharsis region constitutes a long-lived magmatic province, with construction probably occurring early in Martian history (> 3.5 Ga; Mouginis-Mark et al., 2021; Werner, 2009). Based on the summit caldera-based reconstructions of major Tharsis volcanoes (e.g., Tharsis Tholus and Ascraeus Mons; Robbins et al., 2011), the magmatic activity was probably continuous through the Amazonian (< 3.0 Ga; Robbins et al., 2011; Werner, 2009) with the most recent activity, located on the flanks of Olympus Mons dated to 2.4 Ma (Neukum et al., 2004). The Amazonian-age volcanism in Tharsis (from at least 2.4 Ga until at least 330 Ma) was likely sourced by a continuously active superplume that is deep-seated in the mantle, since the beginning of the Tharsis formation (Lagain et al., 2021). The continuity of volcanic and thus magmatic activity in Tharsis throughout the last 1 Ga is further supported by individual older distributed volcanoes (Hauber et al., 2011; Pieterek et al., 2022). However, the majority of older (> 500 Ma) distributed volcanoes have been probably buried under younger (Late Amazonian; < 300 Ma) and wide-spread plain style volcanism (Brož and Hauber, 2011). The volcanic activity of late Amazonian age (< 100 Ma) has been documented across the entire Tharsis (Pieterek et al., 2022), especially in the vicinity of Olympus Mons, Alba Mons, and Pavonis Mons (Bleacher et al., 2007; Hauber et al., 2011; Pieterek et al., 2022).

Here, our studied region is situated to the southeast of Pavonis Mons and north of Noctis Labyrinthus (Fig. 1a) and the general topography gradually decreases in elevation from the southwest to the northeast. This background topography is well expressed by the elongation direction of the nearby lava flows (Fig. 1b). In particular, the region of interest is characterized by a set of volcanic features such as central volcanic fissure vents and accompanied low shield volcanoes that belong to the Pavonis-related cluster of distributed volcanoes (Fig. 1b). Although, the entire volcanic field constitutes a part of a much

larger system of distributed volcanism (Pieterek et al., 2022), here, we conducted the spatiotemporal reconstruction of volcanic activity mainly focusing on the prominent fissure (green triangle no. 1; Fig. 1b) and its associated volcanic units (vu) no. 1, 3, and 8. The adjacent mapped and studied volcanic units constitute the crucial geological context that allowed us to provide detailed constraints for our research.

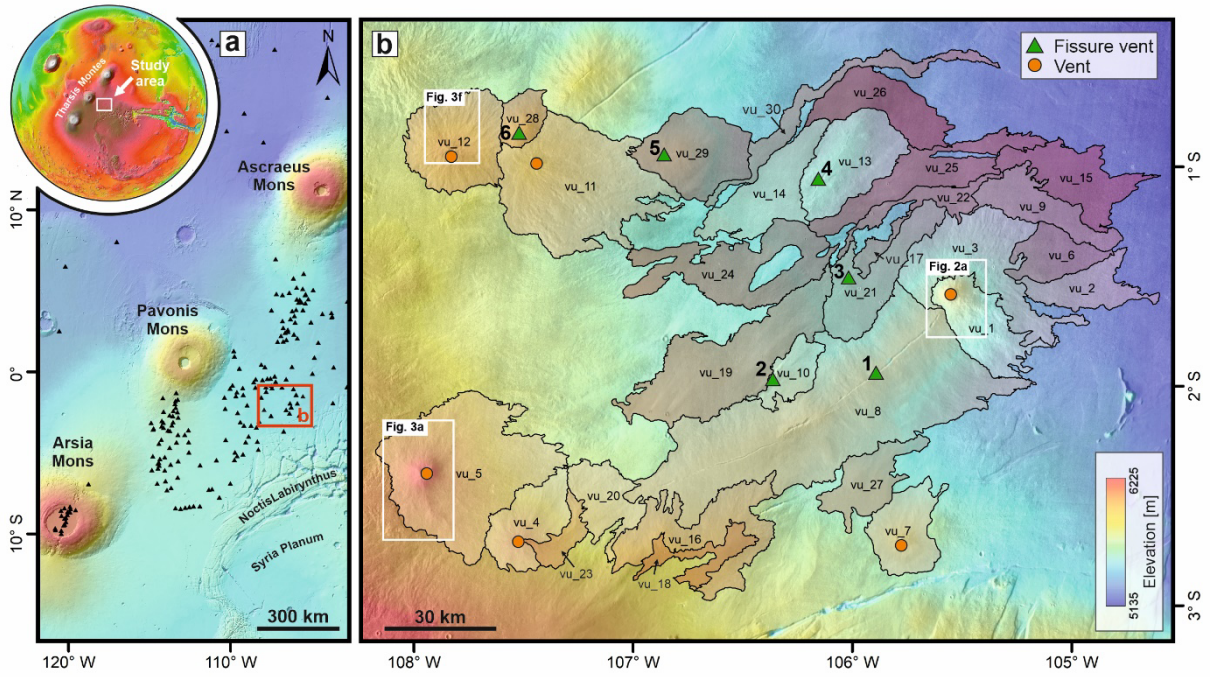

Fig. 1 Studied volcanic field located to the southeast of the Pavonis Mons volcano. (a) An overview map of the Tharsis Montes region with the previously (Pieterek et al., 2022) mapped distributed volcanoes (black triangles). The top left inset shows the topographic map of Mars with the white rectangle indicating the location of the study area. **(b)** Topographic map of the studied volcanic field with the 30 volcanic units (e.g., vu_1) that have been mapped and dated as part of this study. Units are shaded according to stratigraphic position, with lower units being darker and overlying units being lighter in colour. The green triangles indicate the approximate centre of the exposed fissure vents, whereas orange circles mark the locations of vents. In both panels, the base map is a blend of digital elevation model (200 m/px; Fergason et al., 2018) data derived from the Mars Orbiter Laser Altimeter (MOLA) and High-Resolution Stereo Camera (HRSC) and a global daytime infrared mosaic of the Thermal Emission Imaging System (THEMIS) (100 m/px; Edwards et al., 2011).

Methods

Mapping volcanic units

To conduct a detailed mapping and dating of the volcanic landforms and associated lava flow units, we used the Context Camera images (CTX; Malin et al., 2007) onboard the Mars Reconnaissance Orbiter (MRO). CTX images have a spatial resolution of ~ 5 m/px (Table S1), which is sufficient to identify the spatial extent of the mapped landforms, their structural relationship with the adjacent units, and to count impact craters used for age determination. To provide detailed observations at the local scale, we also used High Resolution Imaging Science Experiment (HiRISE; McEwen et al., 2007)

images (also onboard MRO) for selected areas with a spatial resolution of 25–52 cm/px (Table S2). The elevation data for the entire study area were acquired from a blended digital elevation model (200 m/px; Fergason et al., 2018) derived from the Mars Orbiter Laser Altimeter (MOLA; Smith et al., 2001) and the High-Resolution Stereo Camera (HRSC; Gwinner et al., 2016). To conduct a detailed topographic analysis of region of interest, we used digital elevation models (DEMs) derived from both CTX and HiRISE stereo pair images (Table S2). To achieve this, we used the data processing information system, MarsSI (Mars System of Information) (Quantin-Nataf et al., 2018). The CTX-based DEMs have a spatial scale of ~ 12 m/px and a vertical resolution of ~ 4 m allowing us to conduct precise topographic measurements and reveal the overlying relationship between the mapped volcanic units and thus provide stratigraphic constraints. In the case of an uncertain stratigraphic relationship, we mapped adjacent volcanic units to maintain at least two contacting units to determine relative stratigraphy. To support our stratigraphic interpretation, we determined the surface ages of the areas representing an individual volcanic event or multiple events associated with the same volcanic landform, for example, a single period of lava effusion represented in the deposit record by a single lava flow unit (e.g., vu_1). The outlines of the dated areas were determined based on the geological contacts of the region of interest. Morphology was visualized using CTX images and supported by the elevation data. All image and data analysis associated with mapping were conducted using ArcGIS software version ArcMap 10.5.

Age dating

Although the studied region represents a complex volcanic system characterized by multiple eruptions, we attempted to reconstruct the eruptive sequence in both time and space. To achieve this, we dated 30 volcanic units ranging in area from ~ 69 to ~ 2506 km^2 (Table S3). In total, we mapped ~ 7,800 impact craters for the entire set of dated units, from which ~50% have been used for fitting isochrones (~ 3,900). The number of impact craters used for fitting Crater Size-Frequency Distributions (CSFDs) with isochrons varies from 15 to 600 (Table S3 and Figs. S1-S30). In the planetary scientific community, there is still ongoing discussion about the minimum area and crater sizes usable for reliable dating (Lagain et al., 2021; Warner et al., 2015; Werner, 2009). For example, Warner et al. (2015) suggested that because of the heterogeneous pattern of cratering over 100 km^2 regions and resurfacing processes, crater counts derived from small areas (from 100 to 1000 km^2) might be suspected to large uncertainties. However, although our dated areas vary greatly in size (some of the units below or close the minimum threshold of 100 km^2; Warner et al., 2015) and thus the number of impact craters, we did not observe any bias in obtained ages related to area size nor any correlation between the obtained ages and the number of fitted craters used (Fig. S31). Such correlation could be interpreted as a bias due to crater obliteration by erosion processes (Lagain et al., 2020) and this was not observed here. The age of each volcanic unit was estimated based on crater counting methods using diameters > 50 m (the exact minimum diameter of impact craters varies depending on the randomness analysis; Table S3) and by applying the ArcGIS plug-in (Kneissl et al., 2011) CraterTools2.1. Small impact crater diameters on this

order have already been used with success in several studies on volcanic terrains for isochrons fitting based on CTX images (Brož et al., 2017; Hauber et al., 2011; Pieterek et al., 2022; Richardson et al., 2017). Crater statistics and derivation of crater model ages, including errors, were carried out using the CraterStats II software (Michael and Neukum, 2010) (Figs. S1-S30). We fitted the CSFD using the Hartmann (2005) chronology model and the Poisson timing analysis, which allowed us to avoid any bias related to the crater size binning (Michael et al., 2016). In addition, we compared our results using two other chronology systems: Ivanov (2001) and Hartmann and Neukum (2001) (Table S3). Moreover, to evaluate the potential contamination of secondary craters in our counting, the degree of clustering was measured at various crater diameter bins using the Randomness Analysis tool (Michael et al., 2012) within the CraterStats software. A full description of this technique is available in Lagain et al. (2020) and Pieterek et al. (2022). The shapefiles including dated areas, mapped impact craters, and CraterStats files for the entire set of dated areas are attached to this manuscript as Supplementary Data 1.

Results

Mapping of volcanic units

In the studied region, we mapped 30 volcanic units that constitute the volcanic field (Fig. 1). This field contains different volcanic landforms including lava flows associated either with fissure eruptions or low shield volcanoes and (monogenetic) low shield volcanoes with steep summit cones (Figs. 2 and 3). Multiple lava flows are associated with the large ~ 90 km long central NE-SW trending fissure. Herein this fissure is referred to as the central fissure. Volcanic unit number 8 (vu_8) is the largest unit by area, and in its northeastern end is partly covered by two generations of lava flows (Figs. 2a-c). The stratigraphically lower flow (vu_3) consists of hundreds of elongated lava flows that form finger-shaped structures. This vu_3 unit is partly covered by a south-trending lava flow (vu_1), thus vu_1 is stratigraphically the youngest in this region and forms the steep summit cone with NE-SW trending vent (Fig. 2d). Using the High Resolution Imaging Science Experiment (HiRISE) image, in the northeastern part of the summit area, we observed a ridge structure with small mounds that are aligned in the same NE-SW direction as the summit vent and central fissure (Fig. 2d-f). Given their stratigraphic position these mounds are likely to be the youngest volcanic feature, however they are too small to be allocated a separate volcanic unit and accurately age dated (Fig. S32).

Comparative analysis of the volcanic unit surfaces revealed that the summit area of the cone (vu_1) is characterized by a rough and blocky texture relative to the surrounding flows that have a smoother surface texture (Figs. 2c and S33). In addition, the stratigraphically older unit, likely originating from the same summit vent, forms finger-shape lava flows (vu_3). The fissure-associated lava flows, in general, are characterized by smooth surface morphologies (Figs . 2a-c and 4b-c). Based on our DEMs, we can demonstrate that the summit cone raises from ~ 5790 meters to ~ 5980 meters above the Martian datum and has near-summit slopes of ~ 6° that contrasts with the surrounding low-angle slopes of cone-

associated or fissure-associated lava flows that are characterized by lower angle slopes up to 2° (Fig. 2e).

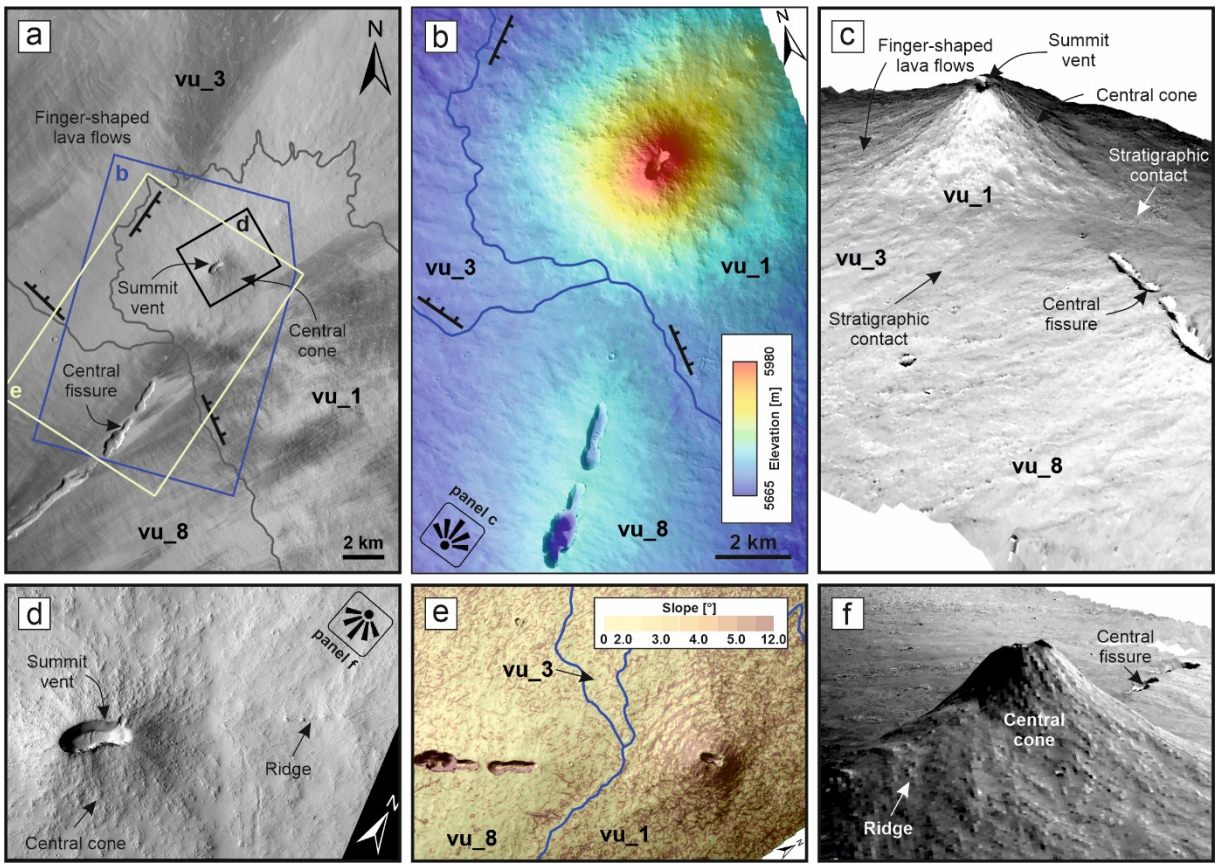

Fig. 2 Morphological characteristics of the northern end of the fissure system. (a) An overview image of the northeastern part of the studied volcanic field characterized by the central cone and associated lava flow units (e.g., vu_1). The lines with hachures (ticks) on the side of the overlying younger flow indicate the stratigraphic relationship between the mapped units. Produced using CTX image G15_023966_1785, centered at 1.53°S, 254.50°E. **(b)** A corresponding topographic map of the region based on the CTX-based stereo-pair digital elevation model (spatial resolution of 12 m/px). CTX stereo-pair images comprise P07_003752_1796 and G13_023333_1785. **(c)** 3D visualization of the central cone and central fissure using the same CTX-based DEM showing distinguishable stratigraphic contacts between the volcanic units. This visualisation is vertically exaggerated 10 times. **(d)** Close-up image of the central cone and summit vent with the NNE-aligned ridge. The cone comprises a blocky-texture and short lava flows. Produced using HiRISE image ESP_023333_1785, centered at 1.594°S, 254.452°E. **(e)** Map showing a difference in slope between the fissure-associated lava flows (vu_8) and central cone superimposed on the fissure (vu_1). **(f)** Corresponding 3D visualization of the central cone and associated ridge. The ridge shows the same alignment as the central fissure. Produced with the same settings as in panel (c).

To the southwest of the central fissure, another topographically prominent volcanic edifice is observed (Fig. 3). Again, a set of fissure-associated flows are overlaid by structurally higher volcanic units associated with a low shield volcano (vu_4; Fig. 5). Moreover, this volcano is also in structural contact with another neighbouring low shield volcano (vu_5) that has steep summit cones with circular-shaped vents (Fig. 3a-e). These cones are ~ 150 meters higher in elevation than the associated flows at their base (Fig. 3a). The cone flanks are formed of finger-shaped lava flows characterized by a rough

and blocky surface texture (Fig. 3d-e). In addition, further to the northwest within the studied region, we documented other low shield volcanoes (vu_11 and 12). These are located to the northwest of the central fissure and are characterized by similar finger-shaped lava flows that originated from summit vents (e.g., Fig. 3f).

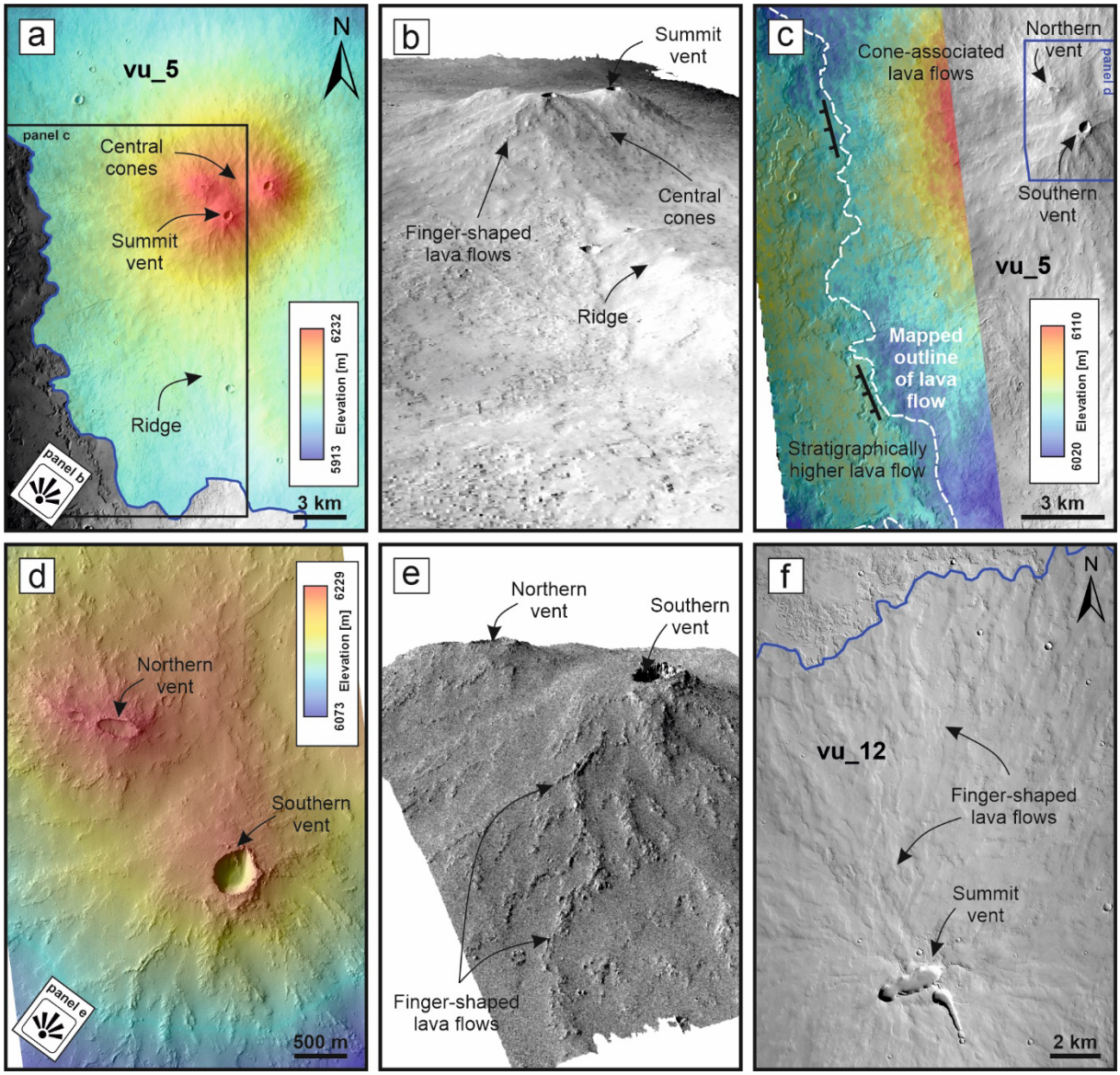

Fig. 3 Morphological characteristics of other low shield volcanoes adjacent to the central fissure. **(a)** Topographic map of the southwestern low-shield volcano (vu_5) with steep summit cones and associated finger-shaped lava flows originating from summit vents. The DEM is based on the CTX stereo-pair images P02_001906_1776 and P03_002117_1776, centered at 2.4°S, 252.06°E. **(b)** Corresponding 3D visualization of vu_5 showing the relatively steep-sloped central cones. On the southern slope of the volcano, there is emplaced elevated ridge. This visualization is 10 times vertically exaggerated. **(c)** Topographic data showing that that the western lava flow is stratigraphically younger relative to the adjacent lava flows originating from the summit vents. The lines with hachures (ticks) on the side of the overlying younger flow indicate the stratigraphically higher unit. **(d)** Close-up HiRISE image of the summit vents of the low-shield volcano (vu_5) blended with the HiRISE-based DEM (HiRISE images PSP_001906_1775 and PSP_002117_1775, centered at 2.4°S, 252.04°E. **(e)** 3D visualization of the features in (d). The visualization is based on the HiRISE-based DEM and is 10 times vertically exaggerated. **(f)** Another low-shield volcano (vu_12) characterized by a complex summit vent

with associated finger-shaped lava flows similar to those described elsewhere in studied volcanic field (c.f., vu_3, 5, and 11; see Figs. 2 and 4). For the geological context, the reader is referred to Figure 1.

Given that the deposits associated with the central fissure (Fig. 2) are not buried by younger volcanic deposits, the vent structures can be examined (Fig. 4a). The fissure vents are not infilled by subsequent lava flows, and the fine-grained deposits such as aeolian dunes cover only the vent floors. The morphology of the central fissure is shown in Figure 4, we observed that along most of its length, it is characterized by sharp margins and steep walls (Fig. 4b-d). Where elevation profiles could be constructed, we observe that the fissure vents have elevated rims and we interpret these to be spatter ramparts (Jones et al., 2018; Wilson et al., 2009). In the central part of the fissure, there is structurally higher vent (i.e., the youngest), superimposed on the central fissure and associated lava flows, and is characterized by irregular margins (Fig. 4e). Similar irregular-margined fissures have also been documented for the adjacent edifice (vu_10; Fig. 4f).

In addition to vent structures, the well-preserved volcanic landforms with clear stratigraphic relationships, especially in the northern end of the fissure, allow us to determine the thickness of the volcanic units including individual lava flows (Fig. S34). We found that the fissure-associated lava flows (vu_8) were overlaid by > 10-m-thick finger-shape lava flows (vu_3) that most likely originated from the summit cone vent. The later shorter distance (probably more-viscous) flows forming the steep summit cone (vu_1) reveal thickness ranging from ~ 11 up to ~ 20 m. Our thickness measurements show that individual lava flow units have a relatively homogeneous thickness but between units range from several (~ 2 m) up to tens (~ 20) meters (Fig. S34).

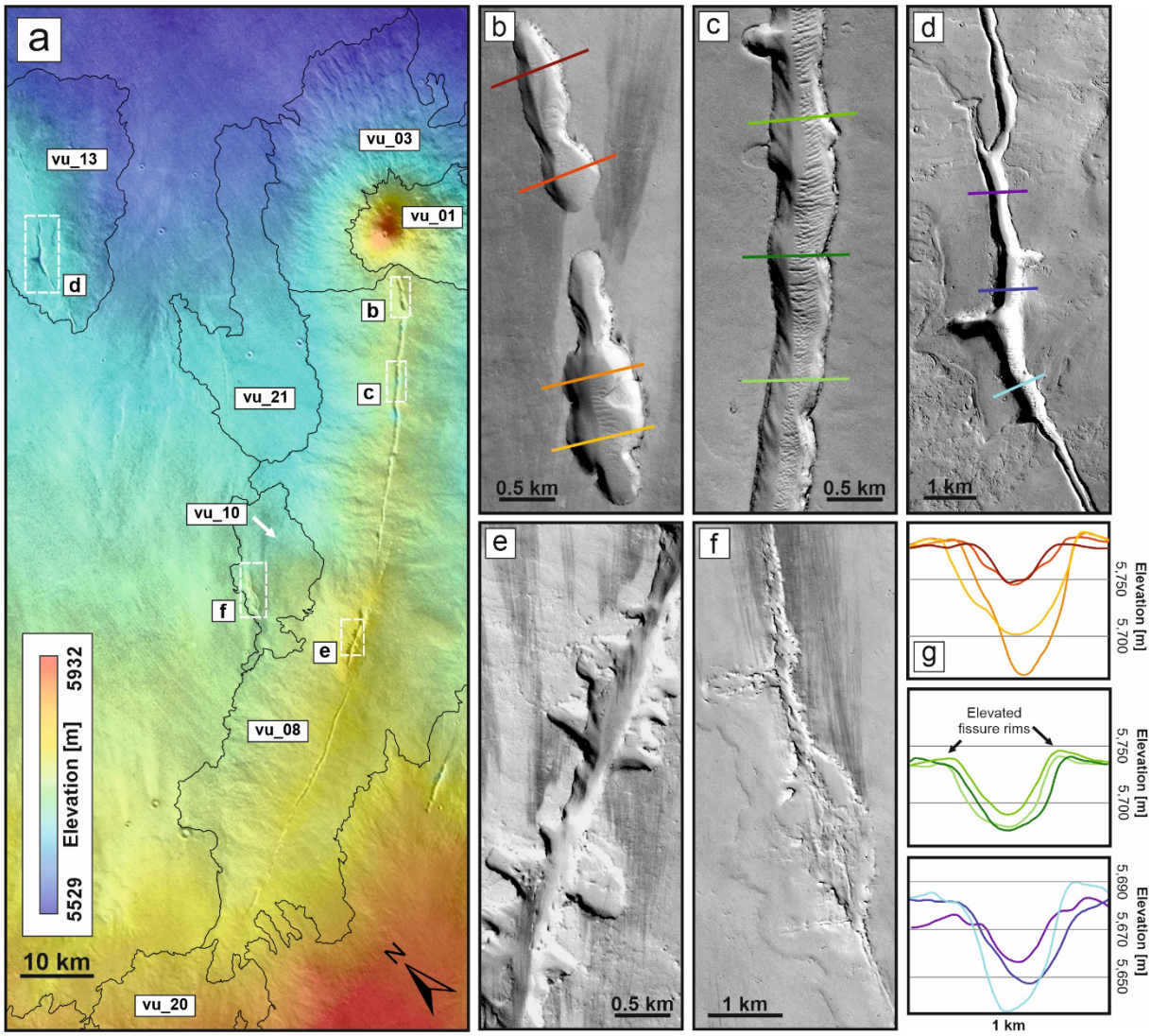

Fig. 4 Vent proximal characteristics of the volcanic fissures. (a) An overview image of the central fissure (vu_8) showing the different vent morphologies along its length. The base map is a combination of the MOLA-HRSC digital elevation model (200 m/px; Fergason et al., 2018) and a global daytime infrared mosaic of THEMIS (100 m/px; Edwards et al., 2011). **(b-d)** Examples of fissure morphologies that show either sharp outlines and steep walls or **(e & f)** irregular margins. Produced using CTX images N14_068050_1788, D12_031891_1789, and G15_023966_1785. All subpanel images have the same orientation as the overview image in panel a. **(g)** Corresponding elevation profiles based on the CTX-based DEMs (CTX stereo pairs P07_003752_1796 and G13_023333_1785 (panel b and d); D12_031825_1789 and D12_031891_1789 (panel c); for details see Table S1). All profiles reveal elevated fissure rims. For the irregular-margined fissures (e & f), the CTX-based DEMs are unavailable. The line colours in the elevation profiles match those drawn on the map (panels b-d).

313 *Age-dating*

314 Each of the mapped units has at least two neighbouring units, which enables us to determine their
315 relative age based on the stratigraphic superposition (Fig. 5). Furthermore, to reconstruct a quantitative
316 temporal evolution of volcanic activity in the studied region, using crater counting, we dated the 30
317 volcanic units (Figs. 5–6 and Figs. S3–32; Table S3). Each volcanic unit represents an individual
318 eruptive event (e.g., a set of lava flows) with a unique age. Remarkably the age order reconstructed by
319 both mapping unit superposition and crater counting determinations perfectly agree (Fig. 6).

320 From crater counting methods we have determined that at least two volcanic eruption events occurred
321 pre-130 Ma, although the apparent eruption frequency did not substantially increase until after 75 Ma
322 (Fig 6 and Table S3). This apparent frequency however could be biased due to the burial of older
323 volcanic units by subsequent eruptions. Based on the age determinations, the lava flows associated with
324 central fissure (vu_8) are 64.3 million years old, whereas the neighbouring flows and edifices are
325 stratigraphically lower (Fig. 5) and have ages ranging from 64.5 (vu_19) to 82.7 Ma (vu_27). The
326 northernmost end of the central fissure hosts a low shield volcano with finger-shaped lava flows exposed
327 on its lower slopes (vu_3; 50.4 Ma) and relatively younger lava flows (i.e. later eruptions) that
328 constructed the steep summit cone (vu_1; 47.3 Ma) (Fig. 5b-c).

329 A similar case is observed in the southwestern end of the study region. The volcanic edifices (i.e.,
330 low shield volcanoes with steep summit cones) are younger (< 60 Ma) and superimposed on older
331 fissure-associated lava flows (Fig. 5). Our obtained ages indicate that all eruptions that constructed the
332 summit vents and cones of low shield volcanoes postdate the associated fissure-fed lava flows.
333 Additionally, the studied area hosts several other volcanic edifices with a similar age to the latest
334 eruption located on the central fissure (vu_4 and 5; Fig. 5). Interestingly, the three low-shield volcanoes
335 (vu_3, 5, and 11) with finger-shaped lava flows on their slopes all have similar eruption ages ranging
336 from 54.1 to 50.4 Ma.

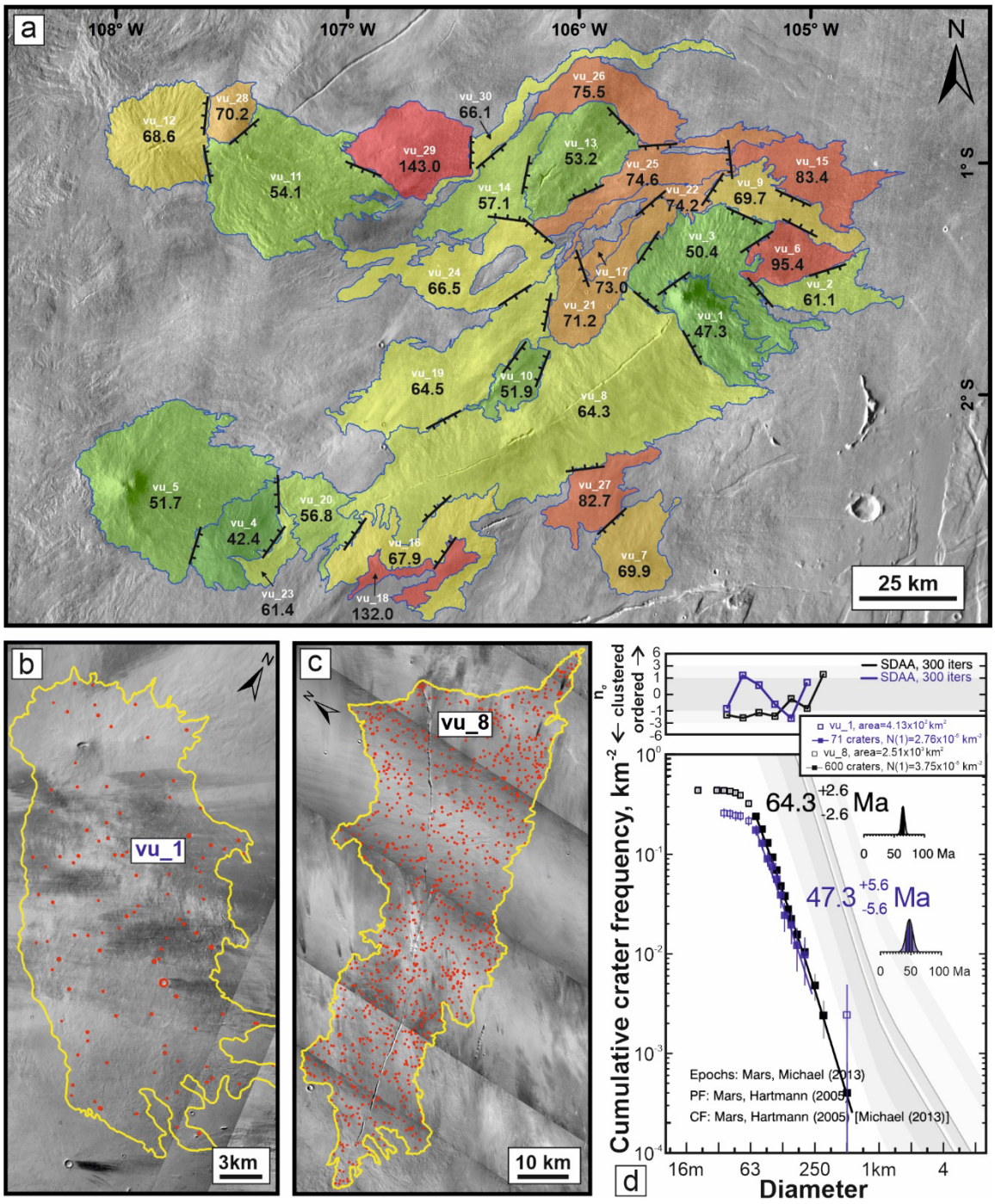

Fig. 5 Ages of the studied volcanic units. (a) The age distribution of the dated units (the youngest units are green, and the increasing age changes the colour towards red). The numbers displayed within the units indicate the obtained ages based on the Hartmann (2005) chronology system and are expressed in millions of years. The lines with hachures (ticks) on the side of the overlying younger flow indicate the stratigraphically higher unit based on mapping relationships. The base map is a global daytime infrared mosaic of THEMIS (100 m/px; Edwards et al., 2011). **(b & c)** Crater counting examples. The dated areas (outlined in yellow) together with the mapped impact craters (red circles) are shown on CTX images (Table S1). **(d)** Corresponding Crater Size-Frequency Distribution plots (CSFD) as well as absolute model ages measured on two volcanic units (for more details see Table S3). The ± error is the 1σ age uncertainty based on the number of craters fitted. The upper panel of the CSFD plot shows the results of randomness analyses using the (inversed) standard deviation of the adjacent area (SDAA) parameter (Michael et al., 2012).

Discussion

Agreement between relative and absolute model ages

The combination of detailed mapping and age-dating determination of volcanic landforms using crater counting constitutes a powerful approach to understand the spatiotemporal evolution of volcanic systems. Here, we showed that all our age-dating results are fully consistent with the superposition relationships between the studied volcanic units (Figs. 5 & 6). In this study, it was essential to decipher the eruption sequence of the volcanic landforms associated with the central fissure. Using CTX-based elevation data and the corresponding 3D models (Fig. 2), we demonstrated that the steep-summit cone (vu_1) is stratigraphically the highest followed by the associated finger-shaped lava flows (vu_3), and lastly, the central fissure lava flows (vu_8; Fig. 5) that are stratigraphically the lowest. These constraints were further verified by crater counting revealing that the central fissure system experienced multiple eruptions of a period of several million years (64.3 through to 47.3 Ma), and thus, likely had a long-lived and active magmatic plumbing system.

The volcanic units within the mapped region that have similar surface appearance, characterized by finger-shape lava flows (vu_03, 05, 11) all reveal close ages by crater counting (51.7–50.4 Ma) indicating their very close temporal association (Fig. 5), and potentially simultaneous eruption. This is interesting for two reasons. First, they are not geographically adjacent and thus cannot be directly related stratigraphically. Therefore, such a temporal relationship indicates multiple eruptions from different, parallel fissures at similar or equivalent times. Second, their common surface character suggests that a similar eruption behaviour and/or magma composition occurred at a common time throughout the entire volcanic field mapped.

Our combined mapping and dating approaches have allowed us to provide a high-resolution spatiotemporal reconstruction of the evolution of a fissure-controlled volcanic system (Fig. 6). To the best of our knowledge, the only similar study was conducted by Richardson et al. (2017) who also used the crater counting method to ground truth their structural observations and reconstruct the volcanic eruptive sequence within the caldera of Arsia Mons. In this study and Richardson et al. (2017), the areas of some of the dated volcanic units were below the minimum threshold (100 km^2) for reliable dating proposed by Warner et al. (2015). In our case, all the ages determined by crater counting are in agreement with stratigraphic position irrespective of the mapped area size (Fig. S31). This suggests that the threshold proposed by Warner et al. (2015) may be more stringent than needed for the Martian volcanic terrains. Therefore we suggest that using areas < 100 km^2 for age dating can be appropriate provided that the results are consistent in the geological context (e.g., supported by stratigraphic relationships). Moreover, in this study, we compared model absolute ages from crater counts performed on the same geological units applying different chronology systems (Table S3). We found that among used chronology systems the obtained results a systematic pattern of ages with the youngest ages for Hartmann and Neukum (2001), middle ages for Ivanov (2001), and oldest ages for Hartmann (2005).

We present these full results in Table S3 to support comparisons between studies using different chronology systems. We argue that such an approach could be successfully applied to other volcanic systems on a larger scale and will provide vital, high-resolution insight into the evolution of magmatic plumbing systems on Mars. The most prominent regions for future investigations are located within Tharsis – regions associated with late Amazonian distributed volcanism that forms complex fields comprising volcanic edifices of polygenetic origin (Hughes et al., 2020).

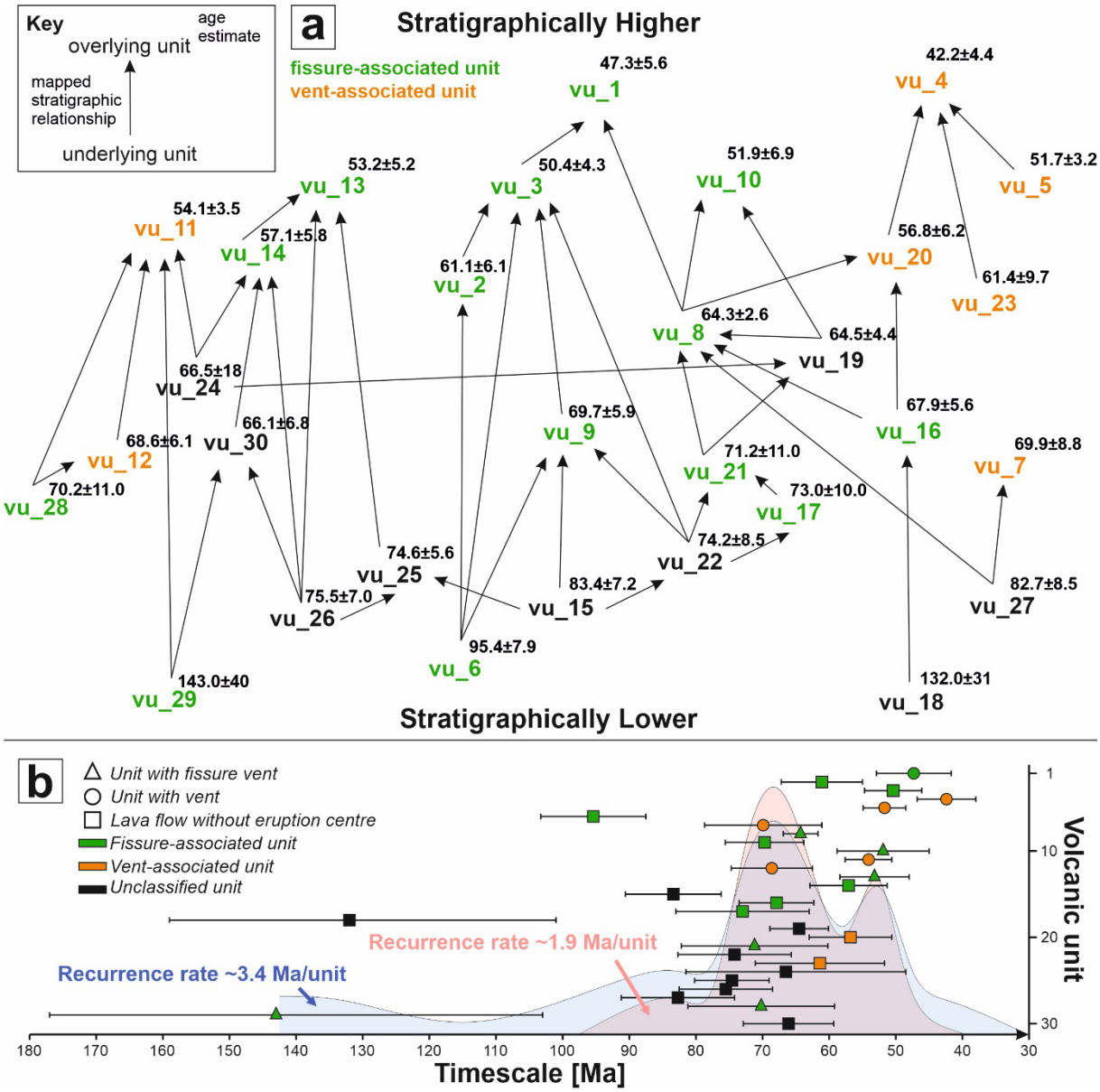

Fig. 6 Temporal evolution of the studied volcanic field. (a) A directed graph of the stratigraphic relationships between mapped units. Units positioned higher graphically (e.g., vu_1) are higher stratigraphically and directly overlie flows that have connecting lines to them (method adapted from Richardson et al. (2017). Each line represents one mapped stratigraphic relationship connecting an overlying unit and an adjacent underlying unit. Age-dating estimates, using crater counting, are given in black superscript and always agree with our observed stratigraphic relationships. **(b)** Absolute ages with errors of the studied volcanic units presented on an actual timescale. The background plots show the frequency of the unit emplacement indicating the clustering of eruption events in time. The y-axis refers to the numbering of the mapped units.

Eruption history and evolution of a fissure system

On Mars, similar to Earth systems, distributed-style volcanism has resulted in the formation of volcanic landforms that are considered to reveal monogenetic origin (Hauber et al., 2009; Németh and Kereszturi, 2015). However, these constraints might be challenged as some of them reveal different morphological characteristics indicating a polygenic character (Bleacher et al., 2007; Hughes et al., 2020). Although Tharsis volcanic evolution has been investigated for decades (Mouginis-Mark et al., 2021; Zimbelman et al., 2015), few studies have conducted detailed spatiotemporal reconstruction of fissure-related volcanic systems. Southeast of Tharsis Montes, there are hundreds of moderate- to small-scale morphologically different volcanic landforms and associated fissures. These fissure vents were formed when the ascending subsurface dykes intersected the surface (Pieterek et al., 2022; Richardson et al., 2021). The magma that fed this volcanism in Tharsis was probably transported in the late Amazonian via radial and circumferential dykes from magmatic plumbing systems generated by long-lasting mantle plumes emplaced beneath central volcanoes (e.g., Arsia Mons, Pavonis Mons, and Ascraeus Mons; Pieterek et al., 2022). Moreover, Hauber et al. (2009) highlighted that volcanic fissures are locally superposed by shield volcanoes indicating their subsequent formation. Here, we were able to reconstruct the eruptive evolution of the volcanic fissure field (Fig. 1) spatially associated with distributed volcanoes. Across the mapped region we found that the volcanic units are erupted every 3.4 Ma on average (Fig. 6b). Furthermore, if the two oldest units are excluded from the recurrence rate calculation, we find that eruptions producing volcanic units occurred every 1.9 Ma. We suggest that this higher recurrence rate is more representative due to the poor preservation of older units as they become buried by later erupted products.

Broadly, fissure eruptions can be classified into two types – monogenetic or polygenetic. The former is characterised by a single volcanic unit associated with a single fissure. Polygenetic fissures on the other hand are characterised by multiple overlapping (i.e., sequential in time) volcanic units. A compound fissure with multiple nested lava flows, spatter and scoria cones is a clear example of a polygenetic fissure (Hughes et al., 2020; Németh and Kereszturi, 2015). Based on this previously proposed classification (Hughes et al., 2020), the Tharsis region on Mars is dominated by seemingly monogenetic fissures that are recently obscured by low shields. However, we show that volcanic system studied here is a compound polygenetic fissure with associated volcanic vents. This complex array of constructional units has allowed us to reconstruct the eruptive evolution of the fissure system. On Earth, it is well known that all fissure eruptions evolve from erupting all along their initial strike to erupting at a series of discrete points, and if the eruption duration is sufficient, they ultimately localize to a single point source, potentially building a cone (Bruce and Huppert, 1990; Jones et al., 2017; Jones and Llewellin, 2021; Moreland et al., 2019; Wylie et al., 1999). Such localization processes are often controlled by the fluid dynamic processes within the feeding dyke system (Jones and Llewellin, 2021). Although for now there are no direct ways to investigate the subsurface dynamics of magma within the

Martian dykes; the only solution is to forensically recover information using surficial observations of volcanic landforms.

Focussing on the central fissure (Figs. 2 and 4) where a large portion of the fissure length is still exposed, we found that the vu_8 lava flows are the oldest amongst the fissure-associated volcanic units. These lava flows cover a large area (~ 2500 km^2) and travelled up to 30 km from the fissure vent. Such characteristics indicate that the initial period of volcanic activity comprised magmas of low viscosity (e.g., high temperature, low crystallinity) and/or were erupted with high mass eruption rates (Hauber et al., 2009; Peters et al., 2021). Later eruptions, again in the form of lava flows, migrated to the NE end portion of the fissure, and resulted in the formation of the low shield volcano characterized by finger-shaped lava flows that travelled similar distances (maximum ~ 25 km) to the fissure-associated lava flows. The youngest dated volcanic unit (vu_1) constitutes the uppermost part of the low shield volcano and forms the steep-summit cone (Fig. 2). The lavas associated with this summit cone only travel a relatively short distance from the vent (from 5 to 10 km). These observations are in agreement with localization and channelization processes within the dyke system proposed for terrestrial systems (Bruce and Huppert, 1990; Jones and Llewellin, 2021; Wylie et al., 1999).

Furthermore, in addition to our observations, it has previously been suggested (Hauber et al., 2009) that the small-scale mounds forming the elongated ridge (Fig. 2d) might be spatter cones suggesting presence of relatively cooled and viscous magma during dwindling stages of the last eruption. These were too small in areal extent to be mapped as a separate volcanic unit and reliably dated in this study, but they are stratigraphically the highest. This indicates that they formed after, or simultaneously with the steep-summit cone (Fig. S32). Thus, they represent the final period of eruptive activity along this central fissure. In terrestrial fissure systems, such evolution might be also tracked by chemical analyses and petrographic observations of the erupted material. However, in the case of Martian research, the available CRISM data (Compact Reconnaissance Imaging Spectrometer for Mars onboard Mars Reconnaissance Orbiter) are insufficient to reveal any significant difference that would support our observations and results on magma differentiation.

Additionally, the other low shield volcano with steep summit cones (vu_5; Fig. 3) located to the SW of the central fissure, has a similar age to the volcanic units superimposed on the central fissure (vu_1, 3) (Fig. 5–6). This lava cone shares morphological similarities to the NE volcanic units (vu_1, 3) such as the presence of steep-summit volcanic edifice, slope textures, and finger-shaped lava flows. We cannot confirm with certainty that they belong to the same plumbing system, however, the morphological and temporal similarity between these different low shield volcanoes (e.g., vu_3, 5, 11–12) indicates their geological affinity controlled by similar eruptive conditions and/or magma composition.

Evolution of dyke and plumbing system

Our multi-approach study provides one of the first attempts to reconstruct the evolution of a dyke-fed Late Amazonian volcanic field. Here, we demonstrated that the youngest lava flows (47.3 and 42.4 Ma), are associated with localized eruptions of dyke-fed volcanism. We have shown that the central fissure initially erupted low-viscosity magmas all along the fissure strike, potentially with high effusion rates and progressively, over the course of millions of years (Fig. 5), the eruptions became localized to a singular point source at the end of the NE segment now exposed (Fig. 2). The later localized eruptions built up the low shield volcano comprising finger-shape lava flows (vu_3), and in the final stage of volcanic activity built the steep-summit cone (vu_1). These final lavas responsible for low shield volcano and summit cone construction reveal different surface characteristics compared to fissure-associated lava flows (Fig. S33). The volcanic unit (vu_3) preceding the formation of the summit cone comprises highly lobate (finger-shape) lava flows, whereas the flanks of the summit cone are rough with blocky texture. These morphologies could indicate the eruption of magmas of higher viscosity (e.g., higher crystal content, colder and/or more chemically evolved). Together, these observations of progressive localization and the increase in viscosity of erupted products suggest that, over time, this fissure system had a plumbing system that was long-lived (minimum $\gtrsim$ 9 Ma), experienced progressive subsurface flow focussing, and evolved chemically by crystallization and/or magmatic differentiation. Thus, the reconstruction of plumbing systems in this way can provide vital information about the continuity of melt supply and the frequency of related volcanic activity.

Comparing our ages of emplacement (e.g., youngest eruptions of 47.3 and 42.4 Ma) with other volcanic regions in Tharsis (Hauber et al., 2011; Pieterek et al., 2022), the studied area comprises some of the youngest volcanic activity, especially southeast of Tharsis Montes. The most recent regional spatiotemporal reconstruction of volcanic edifices in Tharsis showed that among three volcanoes of Tharsis Montes, Pavonis Mons reveals the youngest ages of volcanic unit emplacement (for more details the reader is referred to Figure 7 and Table 3 in Pieterek et al., 2022). This implies that Mars has retained the capability of producing substantial volcanism. Using 3-D thermal evolution models (Plesa et al., 2023), it has been suggested that the formation of prominent, long-lived mantle plumes underneath Tharsis, were stable in the Amazonian and still produce melt today. Furthermore, assuming two different crustal scenarios (Plesa et al., 2023), it has been inferred that the highest present-day melt fraction zones are beneath southeast of Tharsis Montes – the location of our study. Thus, we suggest that these melt-rich zones might have constituted the source of melt that supplied the dyke-fed volcanic field studied here. Our study, and the use of high-resolution mapping, can therefore provide a vital insight into the subsurface plumbing system and constitutes a ground truth for current melt generation.

Comparative analyses with terrestrial systems

Although the physical and atmospheric conditions are different, it is useful to compare our observations of Martian volcanism with Earth-based volcanic eruptions (Table 1). On Earth, giant dyke swarms are interpreted to be an important component of the plumbing systems of large igneous provinces (LIPs; Buchan and Ernst, 2019) and they also likely controlled the Martian distributed volcanism in Tharsis (Pieterek et al., 2022). Therefore, we compared the studied volcanic field with both terrestrial Hawaiian-style basaltic fissure systems and with LIPs. As shown in Table 1, our fissure-controlled volcanic field shares more similarities with typical LIPs than with Hawaiian-style basaltic fissure systems. However, in general, Martian landforms are larger than LIPs, potentially indicating that a higher magma influx into the plumbing systems has allowed Martian systems to remain active longer.

Table 1 Comparative analysis between the studied fissure-controlled volcanic field and terrestrial systems.

Parameter	Mars (this study)	Basaltic fissure eruption	References	Large Igneous Provinces	References
Length of fissure/vent (at surface) [km]	~ 90 (vu_8)	from 1's to 10's of km	(Gudmundsson, 2016) and references therein	from metres to tens (~ 30) of kilometres	(Black et al., 2021)
Fissure/vent width (at surface) [m]	415 (vu_8)	average 0.5 to 4 m from 0.05 up to 40 m	(Dvorak and Eodesy, 1997; Opheim and Gudmundsson, 1989; Parcheta et al., 2015)	100–200 m (occasionally more)	(Buchan and Ernst, 2019) and references therein
Areal extent of products [km^2]	3,650 (vu_1, 3, 8)	100–2500 (Iceland)	(Gudmundsson, 2016; Thordarson and Höskuldsson, 2008)	from 10^2 to 10^6	(Black et al., 2021)
System duration [years]	$9x10^6$ (vu_1, 3, 8)	~5 (Mauna Ulu, Hawai'i)	(Swanson et al., 1979; Tilling et al., 1987)	typical < $1x10^6$ up to ~ $10x10^6$ (continental) up to ~ $40x10^6$ (oceanic)	(Black et al., 2021) and references therein

Fissure system duration is a difficult property to compare as it is hindered by the different observation methods deployed on Mars and Earth. On Earth, in many cases, eruptions are monitored and supplemented with eye-witness accounts. This has allowed us to document eruptions with high temporal resolution (e.g., subdividing a single eruption into multiple phases and further dividing these phases into eruptive episodes that may individually last minutes to hours). This timescale of observation is clearly not possible on Mars. Thus, to allow for a fair and consistent timescale comparison, we define the lifetime of a single interconnected fissure, termed here a fissure system. In our mapped area on Mars, this consists of volcanic units (vu_1, 3, and 8) as they comprise the erupted products clearly associated with the central fissure. These units span a time period ranging from 8.8 to 25.2 Ma (assuming uncertainty of age determinations). On Earth, a good example of a fissure system is the 1969-74 Mauna Ulu eruption in Hawaii (Swanson, 1973; Tilling et al., 1987). This eruption located on the East Rift Zone

(ERZ) of Kīlauea volcano, Hawai‘i, started as a set of interconnected fissure segments and over the course of ~ 5 years progressively built up the Mauna Ulu shield (Fig. 7).

Thus, when comparing our Martian fissure system with basaltic fissure eruptions on Earth, the timescale of eruptive activity along fissure systems on Mars is much greater than on Earth. Even for LIPs, typical system durations are expected to be < 1 Ma and are therefore still shorter than the Martian fissure system investigated here. Perhaps the best terrestrial analogue to the Martian timescales documented here is the timescale associated with the evolution of an entire volcanic system (Walker, 1993) (e.g., the fixed lifetime of a volcano associated with movement away from the hotspot focus). For the Hawaiian Islands this occurs on timescales ranging from ~ 0.1 to ~ 5 Ma, however for hotspot-fed volcanoes situated on slow moving tectonic plates, such as the Canary Islands and Cape Verde Islands the timescales are longer, lasting up to approximately 28 Ma (Meyzen et al., 2015). This entire volcanic system timescale is therefore comparable to the Martian fissure system timescale documented here. The lack of plate tectonics on Mars and the presence of mantle plumes within the Tharsis region may explain the fascinating multi-million-year lifetime of Martian fissure systems. Our constraints provide critical insights into the eruptive evolution of Martian igneous systems, and we suggest that even seemingly simple ‘monogenic’ eruptions need to be revaluated with high-resolution mapping to truly reveal their long-lived, potentially polygenetic, character.

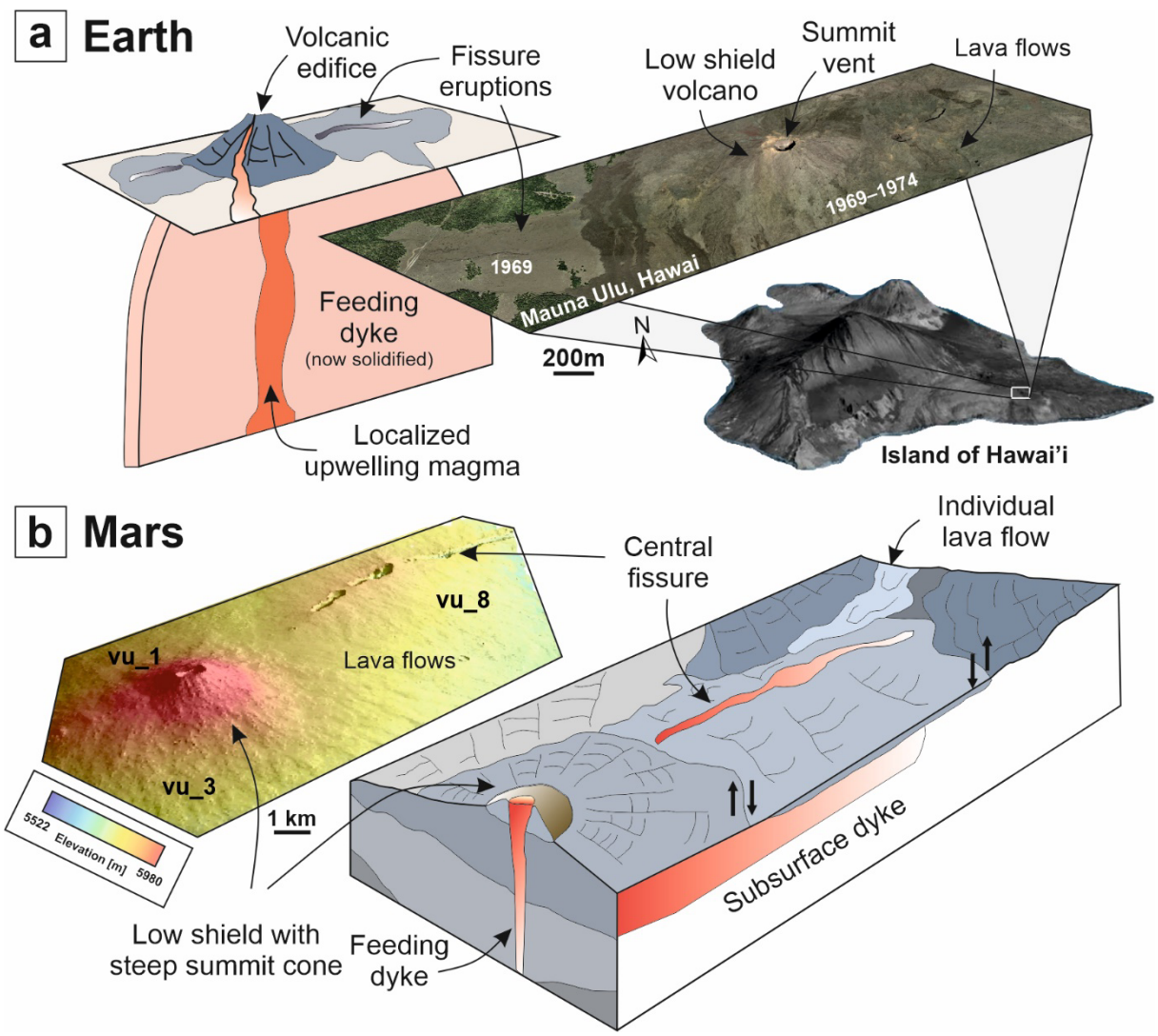

Fig. 7 Schematic models of the dyke-fed plumbing systems on Earth and Mars. (a) A terrestrial example of the Mauna Ulu eruption and associated deposits on Hawai'i. The cartoon of a simplified subsurface plumbing system shows a now localized point of magma upwelling within an originally high aspect ratio dyke. (Google Earth image, Airbus satellite, centered at 19°22'11" N and 155°11'49" W). **(b)** Our dyke-fed volcanic system (south of Pavonis Mons, Mars) presented in the 3D visualization (CTX-based DEM, vertically exaggerated 5 times) and characterized by a volcanic fissure and a low shield volcano with a steep summit cone (for more details, see Fig. 2). The schematic model has been modified from Greeley (1982).

Conclusions

We present the first evidence for the progressive eruption evolution of an individual fissure system on Mars. Our spatiotemporal reconstruction has documented multiple eruptions along a single fissure system. As shown clearly by the central mapped fissure, initial eruptions occurred along the entire fissure length and through time, over a period of at least ≳ 9 million years, evolved to more localized point source eruptions that built up a low shield volcano and a steep summit cone. These changes in eruption location and style reflect progressive localization and focusing of the magma within the subsurface plumbing system. The wide age range in erupted units reveals a long-lived plumbing system

that fed multiple eruptions (i.e., producing landforms with a polygenetic character). Our results that demonstrate magma focusing within dykes over multi-million-year timescales provides new insights into the evolution of fissure systems on Mars and igneous subvolcanic plumbing systems that cannot be observed directly. We therefore contend that detailed mapping supporting volcanic history reconstruction in space and time constitutes a powerful approach for understanding subvolcanic processes on Mars and might be successfully used for other planetary systems in the future.

Acknowledgments

We thank editor Chiara Maria Petrone, Scott Hughes, and an anonymous reviewer for their thorough and insightful comments that improved the manuscript. BP was financially supported by the project "GEO-INTER-APLIKACJE" – high quality doctoral studies program conducted at the Faculty of Geographical and Geological Sciences of the Adam Mickiewicz University in Poznań no. POWR.03.02.00-00-I027/17 funded by the European Social Fund under the Operational Program Knowledge Education Development and by the Adam Mickiewicz University Foundation in the academic year 2022/2023. TJJ was supported by a UK Research and Innovation (UKRI) Future Leaders Fellowship (MR/W009781/1). Elevation data have been processed using the MarsSI (marssi.univlyon1.fr) application founded by the European Union's Seventh Framework Program (FP7/2007-2013) (ERC Grant Agreement No. 280168).

Author contributions

The project was conceived by B.P. and T.J. The data gathering and the production of graphics were completed by B.P. Both authors contributed to the writing of the paper after an initial draft was prepared by B.P.

Competing interests

The authors declare that they have no known competing financial interests or personal relationships that could have appeared to influence the work reported in this paper.

References

Black, B.A., Karlstrom, L., Mather, T.A., 2021. The life cycle of large igneous provinces. Nat. Rev. Earth Environ. 2, 840–857. https://doi.org/10.1038/s43017-021-00221-4

Bleacher, J.E., Glaze, L.S., Greeley, R., Hauber, E., Baloga, S.M., Sakimoto, S.E.H., Williams, D.A., Glotch, T.D., 2009. Spatial and alignment analyses for a field of small volcanic vents south of Pavonis Mons and implications for the Tharsis province, Mars. J. Volcanol. Geotherm. Res. 185, 96–102. https://doi.org/10.1016/j.jvolgeores.2009.04.008

Bleacher, J.E., Greeley, R., Williams, D.A., Cave, S.R., Neukum, G., 2007. Trends in effusive style at the Tharsis Montes, Mars, and implications for the development of the Tharsis province. J. Geophys. Res. Planets 112, 1–15. https://doi.org/10.1029/2006JE002873

Brown, R.J., Blake, S., Thordarson, T., Self, S., 2014. Pyroclastic edifices record vigorous lava fountains during the emplacement of a flood basalt flow field, Roza Member, Columbia River Basalt Province, USA. GSA Bull. 126, 875–891. https://doi.org/10.1130/B30857.1

Brown, R.J., Manya, S., Buisman, I., Fontana, G., Field, M., Niocaill, C. Mac, Sparks, R.S.J., Stuart, F.M., 2012. Eruption of kimberlite magmas: Physical volcanology, geomorphology and age of the youngest kimberlitic volcanoes known on earth (the Upper Pleistocene/Holocene Igwisi Hills volcanoes, Tanzania). Bull. Volcanol. 74, 1621–1643. https://doi.org/10.1007/s00445-012-0619-8

Brož, P., Hauber, E., 2011. Windows of old fractured crust and associated volcanism in Tharsis, Mars, in: European Planetary Science Congress. p. EPSC-DPS2011-742-1. https://doi.org/10.1029/2011GL047310

Brož, P., Hauber, E., Wray, J.J., Michael, G., 2017. Amazonian volcanism inside Valles Marineris on Mars. Earth Planet. Sci. Lett. 473, 122–130. https://doi.org/10.1016/j.epsl.2017.06.003

Bruce, P.M., Huppert, H.E., 1990. Solidification and melting along dykes by the laminar flow of basaltic magma, in: Ryan, M.P. (Ed.), Magma Transport and Storage. John Wiley & Sons Ltd., pp. 87–101.

Bruce, P.M., Huppert, H.E., 1989. Thermal control of basaltic fissure eruptions. Nature 342, 665–667. https://doi.org/doi.org/10.1038/342665a0

Buchan, K.L., Ernst, R. E., 2019. Giant Circumferential Dyke Swarms: Catalogue and Characteristics, in: Srivastava, R.., Ernst, Richard E., Peng, P. (Eds.), Dyke Swarms of the World: A Modern Perspective. Springer Nature Singapore Pte Lts., pp. 1–44. https://doi.org/doi.org/10.1007/978-981-13-1666-1_1

Cocchi, L., De Ritis, R., Casalbore, D., Romagnoli, C., Lucchi, F., Tranne, C.A., Ventura, G., 2019. Seamount-Volcanic Island Transition and Evolution From Fissural to Central Activity Inferred by the Magnetic Modeling of Salina Island (Tyrrhenian Sea). J. Geophys. Res. Solid Earth 124, 4323–4342. https://doi.org/10.1029/2018JB017113

de Silva, S., Lindsay, J.M., 2015. Chapter 15 - Primary Volcanic Landforms, in: Sigurdsson, H. (Ed.), The Encyclopedia of Volcanoes. Academic Press, Amsterdam, pp. 273–297. https://doi.org/10.1016/B978-0-12-385938-9.00015-8

Dvorak, J.J., Eodesy, G., 1997. Volcano geodesy: the search for magma reservoir and the formation of eruptive events. Rev. Geophys. 35, 343–384. https://doi.org/10.1029/97RG00070

Edwards, C.S., Nowicki, K.J., Christensen, P.R., Hill, J., Gorelick, N., Murray, K., 2011. Mosaicking of global planetary image datasets: 1. Techniques and data processing for Thermal Emission Imaging System (THEMIS) multi-spectral data. J. Geophys. Res. E Planets 116, 1–21. https://doi.org/10.1029/2010JE003755

Fergason, R.L., Hare, T.M., Laura, J., 2018. HRSC and MOLA Blended Digital Elevation Model at 200m v2. [WWW Document]. Astrogeology PDS Annex. U.S. Geol. Surv. URL

http://bit.ly/HRSC_MOLA_Blend_v0

Gansecki, C., Lee, R.L., Shea, T., Lundblad, S.P., Hon, K., Parcheta, C., 2019. The tangled tale of Kīlauea's 2018 eruption as told by geochemical monitoring. Science (80-.). 366, eaaz0147. https://doi.org/10.1126/science.aaz0147

Gonnermann, H.M., Manga, M., 2007. The fluid mechanics inside a volcano. Annu. Rev. Fluid Mech. 39, 321–356. https://doi.org/10.1146/annurev.fluid.39.050905.110207

Greeley, R., 1982. The Snake River Plain, Idaho: representative of a new category of volcanism. J. Geophys. Res. 87, 2705–2712. https://doi.org/10.1029/JB087iB04p02705

Gudmundsson, A., 2016. The mechanics of large volcanic eruptions. Earth-Science Rev. 163, 72–93. https://doi.org/10.1016/j.earscirev.2016.10.003

Gwinner, K., Jaumann, R., Hauber, E., Hoffmann, H., Heipke, C., Oberst, J., Neukum, G., Ansan, V., Bostelmann, J., Dumke, A., Elgner, S., Erkeling, G., Fueten, F., Hiesinger, H., Hoekzema, N.M., Kersten, E., Loizeau, D., Matz, K.D., McGuire, P.C., Mertens, V., Michael, G., Pasewaldt, A., Pinet, P., Preusker, F., Reiss, D., Roatsch, T., Schmidt, R., Scholten, F., Spiegel, M., Stesky, R., Tirsch, D., Van Gasselt, S., Walter, S., Wählisch, M., Willner, K., 2016. The High Resolution Stereo Camera (HRSC) of Mars Express and its approach to science analysis and mapping for Mars and its satellites. Planet. Space Sci. 126, 93–138. https://doi.org/10.1016/j.pss.2016.02.014

Hartmann, W.K., 2005. Martian cratering 8: Isochron refinement and the chronology of Mars. Icarus 174, 294–320. https://doi.org/10.1016/j.icarus.2004.11.023

Hartmann, W.K., Neukum, G., 2001. Cratering chronology and the evolution of Mars. Space Sci. Rev. 96, 165–194. https://doi.org/10.1023/A1011945222010

Hauber, E., Bleacher, J., Gwinner, K., Williams, D., Greeley, R., 2009. The topography and morphology of low shields and associated landforms of plains volcanism in the Tharsis region of Mars. J. Volcanol. Geotherm. Res. 185, 69–95. https://doi.org/10.1016/j.jvolgeores.2009.04.015

Hauber, E., Brož, P., Jagert, F., Jodowski, P., Platz, T., 2011. Very recent and wide-spread basaltic volcanism on Mars. Geophys. Res. Lett. 38, 1–5. https://doi.org/10.1029/2011GL047310

Houghton, B.F., Wilson, C.J.N., Del Carlo, P., Coltelli, M., Sable, J.E., Carey, R., 2004. The influence of conduit processes on changes in style of basaltic Plinian eruptions: Tarawera 1886 and Etna 122 BC. J. Volcanol. Geotherm. Res. 137, 1–14. https://doi.org/10.1016/j.jvolgeores.2004.05.009

Hughes, S.S., Garry, W.B., Sehlke, A., Christiansen, E.H., Kobs Nawotniak, S.E., Sears, D.W.G., Elphic, R.C., Lim, D.S.S., Heldmann, J.L., 2020. Basaltic fissure types on Earth: Suitable analogs to evaluate the origins of volcanic terrains on the Moon and Mars? Planet. Space Sci. 193, 105091. https://doi.org/10.1016/j.pss.2020.105091

Ida, Y., 1992. Width change of a planar magma path: implication for the evolution and style of volcanic eruptions. Phys. Earth Planet. Inter. 74, 127–138. https://doi.org/https://doi.org/10.1016/0031-9201(92)90004-F

Ivanov, B.A., 2001. Mars/Moon cratering rate ratio estimates. Space Sci. Rev. 96, 87–104. https://doi.org/10.1023/A:1011941121102

Jones, T.J., Houghton, B.F., Llewellin, E.W., Parcheta, C.E., Höltgen, L., 2018. Spatter matters-distinguishing primary (eruptive) and secondary (non-eruptive) spatter deposits. Sci. Rep. 8, 1–12. https://doi.org/10.1038/s41598-018-27065-1

Jones, T.J., Le Moigne, Y., Russell, J.K., Williams-Jones, G., Giordano, D., Dingwell, D.B., 2022. Inflated pyroclasts in proximal fallout deposits reveal abrupt transitions in eruption behaviour. Nat. Commun. 13, 1–12. https://doi.org/10.1038/s41467-022-30501-6

Jones, T.J., Llewellin, E.W., 2021. Convective tipping point initiates localization of basaltic fissure eruptions. Earth Planet. Sci. Lett. 553, 116637. https://doi.org/10.1016/j.epsl.2020.116637

Jones, T.J., Llewellin, E.W., Houghton, B.F., Brown, R.J., Vye-Brown, C., 2017. Proximal lava drainage

controls on basaltic fissure eruption dynamics. Bull. Volcanol. 79, 1–15. https://doi.org/10.1007/s00445-017-1164-2

Kneissl, T.A., Gasselt, S. Van, Neukum, G., 2011. Map-projection-independent crater size-frequency determination in GIS environments — New software tool for ArcGIS. Planet. Space Sci. 59, 1243–1254. https://doi.org/10.1016/j.pss.2010.03.015

Lagain, A., Benedix, G.K., Servis, K., Baratoux, D., Doucet, L.S., 2021. The Tharsis mantle source of depleted shergottites revealed by 90 million impact craters. Nat. Commun. 12, 6352. https://doi.org/10.1038/s41467-021-26648-3

Lagain, A., Bouley, S., Baratoux, D., Costard, F., Wieczorek, M., 2020. Impact cratering rate consistency test from ages of layered ejecta on Mars. Planet. Space Sci. 180, 104755. https://doi.org/10.1016/j.pss.2019.104755

Lara, L.E., Moreno, H., Naranjo, J.A., Matthews, S., Pérez de Arce, C., 2006. Magmatic evolution of the Puyehue-Cordón Caulle Volcanic Complex (40° S), Southern Andean Volcanic Zone: From shield to unusual rhyolitic fissure volcanism. J. Volcanol. Geotherm. Res. 157, 343–366. https://doi.org/10.1016/j.jvolgeores.2006.04.010

Malin, M.C., Bell, J.F., Cantor, B.A., Caplinger, M.A., Calvin, W.M., Clancy, R.T., Edgett, K.S., Edwards, L., Haberle, R.M., James, P.B., Lee, S.W., Ravine, M.A., Thomas, P.C., Wolff, M.J., 2007. Context Camera Investigation on board the Mars Reconnaissance Orbiter. J. Geophys. Res. Planets 112, E05S04. https://doi.org/10.1029/2006JE002808

Mangold, N., Loizeau, D., Poulet, F., Ansan, V., Baratoux, D., LeMouelic, S., Bardintzeff, J.M., Platevoet, B., Toplis, M., Pinet, P., Masson, P., Bibring, J.P., Gondet, B., Langevin, Y., Neukum, G., 2010. Mineralogy of recent volcanic plains in the Tharsis region, Mars, and implications for platy-ridged flow composition. Earth Planet. Sci. Lett. 294, 440–450. https://doi.org/10.1016/j.epsl.2009.07.036

Mangold, N., Schmidt, M.E., Fisk, M.R., Forni, O., McLennan, S.M., Ming, D.W., Sautter, V., Sumner, D., Williams, A.J., Clegg, S.M., Cousin, A., Gasnault, O., Gellert, R., Grotzinger, J.P., Wiens, R.C., 2017. Classification scheme for sedimentary and igneous rocks in Gale crater, Mars. Icarus 284, 1–17. https://doi.org/10.1016/j.icarus.2016.11.005

McEwen, A.S., Eliason, E.M., Bergstrom, J.W., Bridges, N.T., Hansen, C.J., Delamere, W.A., Grant, J.A., Gulick, V.C., Herkenhoff, K.E., Keszthelyi, L., Kirk, R.L., Mellon, M.T., Squyres, S.W., Thomas, N., Weitz, C.M., 2007. Mars Reconnaissance Orbiter's High Resolution Imaging Science Experiment (HiRISE). J. Geophys. Res. 112, E05S02. https://doi.org/10.1029/2005JE002605

Meyzen, C.M., Massironi, M., Pozzobon, R., Zilio, L.D., 2015. Are terrestrial plumes from motionless plates analogues to Martian plumes feeding the giant shield volcanoes? Geol. Soc. Spec. Publ. 401, 107–126. https://doi.org/10.1144/SP401.8

Michael, G.G., Kneissl, T., Neesemann, A., 2016. Planetary surface dating from crater size-frequency distribution measurements: Poisson timing analysis 277, 279–285. https://doi.org/10.1016/j.icarus.2016.05.019

Michael, G.G., Neukum, G., 2010. Planetary surface dating from crater size – frequency distribution measurements : Partial resurfacing events and statistical age uncertainty. Earth Planet. Sci. Lett. 294, 223–229. https://doi.org/10.1016/j.epsl.2009.12.041

Michael, G.G., Platz, T., Kneissl, T., Schmedemann, N., 2012. Planetary surface dating from crater size-frequency distribution measurements: Spatial randomness and clustering. Icarus 218, 169–177. https://doi.org/10.1016/j.icarus.2011.11.033

Moreland, W.M., Thordarson, T., Houghton, B.F., Larsen, G., 2019. Driving mechanisms of subaerial and subglacial explosive episodes during the 10th century Eldgjá fissure eruption, southern Iceland. Volcanica 2, 129–150. https://doi.org/10.30909/vol.02.02.129150

Mouginis-Mark, P.J., Crown, D.A., Zimbelman, J.R., Williams, D.A., 2021. 3 - The Tharsis Province,

729 in: Zimbelman, J.R., Crown, D.A., Mouginis-Mark, P.J., Gregg, T.K.P. (Eds.), The Volcanoes of
730 Mars. Elsevier, pp. 36–68. https://doi.org/10.1016/B978-0-12-822876-0.00013-8

731 Neal, C.A., Brantley, S.R., Antolik, L., Babb, J.L., Burgess, M., Calles, K., Cappos, M., Chang, J.C.,
732 Conway, S., Desmither, L., Dotray, P., Elias, T., Fukunaga, P., Fuke, S., Johanson, I.A.,
733 Kamibayashi, K., Kauahikaua, J., Lee, R.L., Pekalib, S., Miklius, A., Million, W., Moniz, C.J.,
734 Nadeau, P.A., Okubo, P., Parcheta, C., Patrick, M.R., Shiro, B., Swanson, D.A., Tollett, W.,
735 Trusdell, F., Younger, E.F., Zoeller, M.H., Montgomery-Brown, E.K., Anderson, K.R., Poland,
736 M.P., Ball, J.L., Bard, J., Coombs, M., Dietterich, H.R., Kern, C., Thelen, W.A., Cervelli, P.F.,
737 Orr, T., Houghton, B.F., Gansecki, C., Hazlett, R., Lundgren, P., Diefenbach, A.K., Lerner, A.H.,
738 Waite, G., Kelly, P., Clor, L., Werner, C., Mulliken, K., Fisher, G., Damby, D., 2019. The 2018
739 rift eruption and summit collapse of Kīlauea Volcano. Science (80-.). 363, 367–374.
740 https://doi.org/10.1126/science.aav7046

741 Németh, K., Kereszturi, G., 2015. Monogenetic volcanism: personal views and discussion. Int. J. Earth
742 Sci. 104, 2131–2146. https://doi.org/10.1007/s00531-015-1243-6

743 Neukum, G., Jaumann, R., Hoffmann, H., Hauber, E., Head, J.W., Basilevsky, A.T., Ivanov, B.A.,
744 Werner, S.C., Van Gasselt, S., Murray, J.B., McCord, T., 2004. Recent and episodic volcanic and
745 glacial activity on Mars revealed by the High Resolution Stereo Camera. Nature 432, 971–979.
746 https://doi.org/10.1038/nature03231

747 Opheim, J.A., Gudmundsson, A., 1989. Formation and geometry of fractures, and related volcanism, of
748 the Krafla fissure swarm, northeast Iceland. Geol. Soc. Am. Bull. 101, 1608–1622.
749 https://doi.org/10.1130/0016-7606(1989)101<1608:FAGOFA>2.3.CO;2

750 Parcheta, C., Fagents, S., Swanson, D.A., Houghton, B.F., Eriksen, T., 2015. Hawaiian Fissure
751 Fountains, in: Carey, R., Cayol, V., Poland, M., Weis, D. (Eds.), Hawaiian Volcanoes: From
752 Source to Surface. https://doi.org/10.1002/9781118872079.ch17

753 Peters, S.I., Christensen, P.R., Clarke, A.B., 2021. Lava Flow Eruption Conditions in the Tharsis
754 Volcanic Province on Mars. J. Geophys. Res. Planets 126. https://doi.org/10.1029/2020JE006791

755 Pieterek, B., Ciazela, J., Lagain, A., Ciazela, M., 2022. Late Amazonian dike-fed distributed volcanism
756 in the Tharsis volcanic province on Mars. Icarus 386, 115151.
757 https://doi.org/10.1016/j.icarus.2022.115151

758 Plesa, A.C., Wieczorek, M., Knapmeyer, M., Rivoldini, A., Bozdag, E., Walterova, M., Knapmeyer-
759 Endrun, B., Kim, D., Broquet, A., Stähler, S., Mittelholtz, A., Breuer, D., Johnson, C.L., Hauber,
760 E., Panning, M., Spohn, T., Lognonné, P., Smrekar, S.E., Banerdt, W.B., InSight Science Team,
761 2023. Insight's constraints on the interior of Mars: Geodynamical models and observations, in:
762 54th Lunar Planetary Science Conference. p. 2212.

763 Quantin-Nataf, C., Lozac, L., Thollot, P., Loizeau, D., Bultel, B., Fernando, J., Allemand, P., Dubuffet,
764 F., Poulet, F., Ody, A., Clenet, H., Leyrat, C., Harrisson, S., 2018. MarsSI: Martian surface data
765 processing information system. Planet. Space Sci. 150, 157–170.
766 https://doi.org/10.1016/j.pss.2017.09.014

767 Richardson, J.A., Bleacher, J.E., Connor, C.B., Glaze, L.S., 2021. Small Volcanic Vents of the Tharsis
768 Volcanic Province, Mars. J. Geophys. Res. Planets 126, e2020JE006620.
769 https://doi.org/10.1029/2020JE006620

770 Richardson, J.A., Wilson, J.A., Connor, C.B., Bleacher, J.E., Kiyosugi, K., 2017. Recurrence rate and
771 magma effusion rate for the latest volcanism on Arsia Mons, Mars. Earth Planet. Sci. Lett. 458,
772 170–178. https://doi.org/10.1016/j.epsl.2016.10.040

773 Robbins, S.J., Di Achille, G., Hynek, B.M., 2011. The volcanic history of Mars: High-resolution crater-
774 based studies of the calderas of 20 volcanoes. Icarus 211, 1179–1203.
775 https://doi.org/10.1016/j.icarus.2010.11.012

776 Siebert, L., Cottrell, E., Venzke, E., Andrews, B., 2015. Chapter 12 - Earth's Volcanoes and Their
777 Eruptions: An Overview, in: Sigurdsson, H. (Ed.), The Encyclopedia of Volcanoes. Academic

778 Press, Amsterdam, pp. 239–255. https://doi.org/10.1016/B978-0-12-385938-9.00012-2

779 Smith, D.E., Zuber, M.T., Frey, H. V., Garvin, J.B., Head, J.W., Muhleman, D.O., Pettengill, G.H.,
780 Phillips, R.J., Solomon, S.C., Zwally, H.J., Banerdt, W.B., Duxbury, T.C., Golombek, M.P.,
781 Lemoine, F.G., Neumann, G.A., Rowlands, D.D., Aharonson, O., Ford, P.G., Ivanov, A.B.,
782 Johnson, C.L., McGovern, P.J., Abshire, J.B., Afzal, R.S., Sun, X., 2001. Mars Orbiter Laser
783 Altimeter: Experiment summary after the first year of global mapping of Mars. J. Geophys. Res.
784 Planets 106, 23,689-23,722. https://doi.org/10.1029/2000JE001364

785 Swanson, D.A., 1973. Pahoehoe flows from the 1969-1971 Mauna Ulu eruption, Kilauea Volcano,
786 Hawai'i. Bull. Geol. Soc. Am. 84, 615–626. https://doi.org/10.1130/0016-
787 7606(1973)84<615:PFFTMU>2.0.CO;2

788 Swanson, D.A., WA, D., DB, J., DW, P., 1979. Chronological narrative of the 1969-71 Mauna Ulu
789 eruption of Kilauea volcano, Hawai. US Geol Surv Prof Pap. 1056.

790 Thordarson, T., Höskuldsson, Á., 2008. Postglacial volcanism in Iceland. Jökull 58, 197–228.
791 https://doi.org/10.33799/jokull2008.58.197

792 Thordarson, T., Self, S., 1993. The Laki (Skaftár Fires) and Grímsvötn eruptions in 1783–1785. Bull.
793 Volcanol. 55, 233–263. https://doi.org/10.1007/BF00624353

794 Tilling, R.I., Christiansen, R.L., Duffield, W.A., Endo, E.T., Holcomb, R.T., Koyanagi, R.Y., Peterson,
795 D.W., Unger, J.D., 1987. The 1972–1974 Mauna Ulu eruption, Kilauea Volcano: an example of
796 quasi-steady-state magma transfer. US Geol Surv Prof Pap 1350, 405–469.

797 Udry, A., Howarth, G.H., Herd, C.D.K., Day, J.M.D., Lapen, T.J., Filiberto, J., 2020. What Martian
798 Meteorites Reveal About the Interior and Surface of Mars. J. Geophys. Res. Planets 125, 1–34.
799 https://doi.org/10.1029/2020JE006523

800 Valentine, G.A., Gregg, T.K.P., 2008. Continental basaltic volcanoes - Processes and problems. J.
801 Volcanol. Geotherm. Res. 177, 857–873. https://doi.org/10.1016/j.jvolgeores.2008.01.050

802 Walker, G.P.L., 1993. Basaltic-volcano systems, in: Prichard, H.M., Alabaster, T., Harris, N.B.W.,
803 Neary, C.R. (Eds.), Magmatic Processes and Plate Tectonic. Geological Society Special
804 Publication, pp. 3–38.

805 Warner, N.H., Gupta, S., Calef, F., Grindrod, P., Boll, N., Goddard, K., 2015. Minimum effective area
806 for high resolution crater counting of martian terrains. Icarus 245, 198–240.
807 https://doi.org/10.1016/j.icarus.2014.09.024

808 Werner, S.C., 2009. The global martian volcanic evolutionary history. Icarus 201, 44–68.
809 https://doi.org/10.1016/j.icarus.2008.12.019

810 Wilson, L., Head, J.W., 1994. Mars: Review and analysis of volcanic erupiton theory and relationships
811 to observed landforms. Rev. Geophys. 32, 221–263. https://doi.org/10.1029/94RG01113

812 Wilson, L., Mouginis-Mark, P.J., Tyson, S., Mackown, J., Garbeil, H., 2009. Fissure eruptions in
813 Tharsis, Mars: Implications for eruption conditions and magma sources. J. Volcanol. Geotherm.
814 Res. 185, 28–46. https://doi.org/10.1016/j.jvolgeores.2009.03.006

815 Wylie, J.J., Helfrich, K.R., Dade, B., Lister, J.R., Salzig, J.F., 1999. Flow localization in fissure
816 eruptions. Bull. Volcanol. 60, 432–440. https://doi.org/10.1007/s004450050243

817 Zimbelman, J.R., Garry, W.B., Bleacher, J.E., Crown, D.A., 2015. Chapter 41 - Volcanism on Mars,
818 Second Edi. ed, The Encyclopedia of Volcanoes. Elsevier. https://doi.org/10.1016/B978-0-12-
819 385938-9.00041-9

Figure captions

Fig. 1 Studied volcanic field located to the southeast of the Pavonis Mons volcano. (a) An overview map of the Tharsis Montes region with the previously (Pieterek et al., 2022) mapped distributed volcanoes (black triangles). The top left inset shows the topographic map of Mars with the white rectangle indicating the location of the study area. **(b)** Topographic map of the studied volcanic field with the 30 volcanic units (e.g., vu_1) that have been mapped and dated as part of this study. Units are shaded according to stratigraphic position, with lower units being darker and overlying units being lighter in colour. The green triangles indicate the approximate centre of the exposed fissure vents, whereas orange circles mark the locations of vents. In both panels, the base map is a blend of digital elevation model (200 m/px; Fergason et al., 2018) data derived from the Mars Orbiter Laser Altimeter (MOLA) and High-Resolution Stereo Camera (HRSC) and a global daytime infrared mosaic of the Thermal Emission Imaging System (THEMIS) (100 m/px; Edwards et al., 2011).

Fig. 2 Morphological characteristics of the northern end of the fissure system. (a) An overview image of the northeastern part of the studied volcanic field characterized by the central cone and associated lava flow units (e.g., vu_1). The lines with hachures (ticks) on the side of the overlying younger flow indicate the stratigraphic relationship between the mapped units. Produced using CTX image G15_023966_1785, centered at 1.53°S, 254.50°E. **(b)** A corresponding topographic map of the region based on the CTX-based stereo-pair digital elevation model (spatial resolution of 12 m/px). CTX stereo-pair images comprise P07_003752_1796 and G13_023333_1785. **(c)** 3D visualization of the central cone and central fissure using the same CTX-based DEM showing distinguishable stratigraphic contacts between the volcanic units. This visualisation is vertically exaggerated 10 times. **(d)** Close-up image of the central cone and summit vent with the NNE-aligned ridge. The cone comprises a blocky-texture and short lava flows. Produced using HiRISE image ESP_023333_1785, centered at 1.594°S, 254.452°E. **(e)** Map showing a difference in slope between the fissure-associated lava flows (vu_8) and central cone superimposed on the fissure (vu_1). **(f)** Corresponding 3D visualization of the central cone and associated ridge. The ridge shows the same alignment as the central fissure. Produced with the same settings as in panel (c).

Fig. 3 Morphological characteristics of other low shield volcanoes adjacent to the central fissure. (a) Topographic map of the southwestern low-shield volcano (vu_5) with steep summit cones and associated finger-shaped lava flows originating from summit vents. The DEM is based on the CTX stereo-pair images P02_001906_1776 and P03_002117_1776, centered at 2.4°S, 252.06°E. **(b)** Corresponding 3D visualization of vu_5 showing the relatively steep-sloped central cones. On the southern slope of the volcano, there is emplaced elevated ridge. This visualization is 10 times vertically exaggerated. **(c)** Topographic data showing that that the western lava flow is stratigraphically younger relative to the adjacent lava flows originating from the summit vents. The lines with hachures (ticks) on the side of the overlying younger flow indicate the stratigraphically higher unit. **(d)** Close-up HiRISE image of the summit vents of the low-shield volcano (vu_5) blended with the HiRISE-based DEM (HiRISE images PSP_001906_1775 and PSP_002117_1775, centered at 2.4°S, 252.04°E. **(e)** 3D visualization of the features in (d). The visualization is based on the HiRISE-based DEM and is 10 times vertically exaggerated. **(f)** Another low-shield volcano (vu_12) characterized by a complex summit vent with associated finger-shaped lava flows similar to those described elsewhere in studied volcanic field (c.f., vu_3, 5, and 11; see Figs. 2 and 4). For the geological context, the reader is referred to Figure 1.

Fig. 4 Vent proximal characteristics of the volcanic fissures. (a) An overview image of the central fissure (vu_8) showing the different vent morphologies along its length. The base map is a combination of the MOLA-HRSC digital elevation model (200 m/px; Fergason et al., 2018) and a global daytime infrared mosaic of THEMIS (100 m/px; Edwards et al., 2011). **(b-d)** Examples of fissure morphologies that show either sharp outlines and steep walls or **(e & f)** irregular margins. Produced using CTX images N14_068050_1788, D12_031891_1789, and G15_023966_1785. All subpanel images have the same

orientation as the overview image in panel a. **(g)** Corresponding elevation profiles based on the CTX-based DEMs (CTX stereo pairs P07_003752_1796 and G13_023333_1785 (panel b and d); D12_031825_1789 and D12_031891_1789 (panel c); for details see Table S1). All profiles reveal elevated fissure rims. For the irregular-margined fissures (e & f), the CTX-based DEMs are unavailable. The line colours in the elevation profiles match those drawn on the map (panels b-d).

Fig. 5 Ages of the studied volcanic units. (a) The age distribution of the dated units (the youngest units are green, and the increasing age changes the colour towards red). The numbers displayed within the units indicate the obtained ages based on the Hartmann (2005) chronology system and are expressed in millions of years. The lines with hachures (ticks) on the side of the overlying younger flow indicate the stratigraphically higher unit based on mapping relationships. The base map is a global daytime infrared mosaic of THEMIS (100 m/px; Edwards et al., 2011). **(b-c)** Crater counting examples. The dated areas (outlined in yellow) together with the mapped impact craters (red circles) are shown on CTX images (Table S1). **(d)** Corresponding Crater Size-Frequency Distribution plots (CSFD) as well as absolute model ages measured on two volcanic units (for more details see Table S3). The ± error is the 1σ age uncertainty based on the number of craters fitted. The upper panel of the CSFD plot shows the results of randomness analyses using the (inversed) standard deviation of the adjacent area (SDAA) parameter (Michael et al., 2012).

Fig. 6 Temporal evolution of the studied volcanic field. (a) A directed graph of the stratigraphic relationships between mapped units. Units positioned higher graphically (e.g., vu_1) are higher stratigraphically and directly overlie flows that have connecting lines to them (method adapted from Richardson et al. (2017). Each line represents one mapped stratigraphic relationship connecting an overlying unit and an adjacent underlying unit. Age-dating estimates, using crater counting, are given in black superscript and always agree with our observed stratigraphic relationships. **(b)** Absolute ages with errors of the studied volcanic units presented on an actual timescale. The background plots show the frequency of the unit emplacement indicating the clustering of eruption events in time The y-axis refers to the numbering of the mapped units.

Fig. 7 Schematic models of the dyke-fed plumbing systems on Earth and Mars. (a) A terrestrial example of the Mauna Ulu eruption and associated deposits on Hawai'i. The cartoon of a simplified subsurface plumbing system shows a now localized point of magma upwelling within an originally high aspect ratio dyke. (Google Earth image, Airbus satellite, centered at 19°22'11" N and 155°11'49" W). **(b)** Our dyke-fed volcanic system (south of Pavonis Mons, Mars) presented in the 3D visualization (CTX-based DEM, vertically exaggerated 5 times) and characterized by a volcanic fissure and a low shield volcano with a steep summit cone (for more details, see Fig. 2). The schematic model has been modified from Greeley (1982).